Nanoporous FePd alloy as multifunctional ferromagnetic SERS-active substrate

(Article begins on next page)

18 October 2024

Journal Name

Multifunctional ferromagnetic and SERS-active nanoporous FePd alloy synthesized via dealloying

Matteo Cialone,[a,b] Federica Celegato,[b] Federico Scaglione,[a] Gabriele Barrera,[b] Deepti Raj,[a] Marco Coisson,[b] Paola Tiberto,[b] and Paola [*a]

Nanoporous materials represent an interesting class of materials, given to their unforeseen mag-netic, mechanical, optical and catalytic properties arising from their network of pores and liga-ments. In particular, palladium-rich nanoporous thin films have been produced by dealloying a polycrystalline $Fe_{75}Pd_{25}$ (at. %) alloy in hydrochloric acid. The depletion of the iron and the surface diffusion of the palladium determines not only an evolution of the morphology and stoi-chiometry of the alloy but moreover a change in the optical and magnetic properties of the system. Concerning the magnetic properties, as the dealloying process proceeds, the system acquires a more isotropic behavior. In a like manner, the surface enhancement of the Raman scattering, that has been proven using bipyridine as a probe molecule, increases with the dealloying time. This enhancement, alongside with the high corrosion resistance and biocompatibility of the FePd al-loys, makes them ideals for being employed as surface enhanced Raman spectroscopy substrates in bio-medical applications. Therefore, this mixture of optical and ferromagnetic properties gives these systems a strong multifunctional connotation, which can pave the way for new applications.

Introduction

Porous and nanoporous materials are an interesting class of mate-rials, which lately have attracted the attention of the materials sci-entist. Surely, nanoporous (NPs) materials own their fame thanks to the high surface-to-volume ratio that distinguishes them from their continuous counterpart. This favourable surface-to-volume ratio makes them suitable for several different applications such as fuel cells[1], capacitors[2], batteries[3], catalysis[4,5], and more in general sensing[6,7].

But not only that, their particular morphology has made them popular also in the field of magnetism, where it has been demonstrated that their exceptional surface extension drastically increases the magnetoelectric effect mediated by liquid elec-trolyte[8]. Moreover, the presence of ligaments, which have di-mensions in the nanometer scale, provides the necessary spa-tial confinement for the generation of surface plasmons and therefore makes nanoporous materials particularly suitable to be used as active substrates for surface-enhanced Raman scattering (SERS)[9], which is one of the most promising methods for the detection of the small concentration of organic molecules and nanoparticles[10,11].

[a] Department of Chemistry and NIS, Universita di Torino, Torino. E-mail: paola.rizzi@unito.it
[b] Instituto Nazionale di Ricerca Metrologica, Division for Metrology of Innovative Ma-terials and Life Sciences, Torino.

All the aforementioned properties made NPs materials perfect candidates for the synthesis of multifunctional materials. Here we focused our attention on bimetallic in particular on an iron palladium alloy. Here, the co-presence of a ferromagnetic element togheter with a noble element boost the possibilities of obtaining multifuncional material, which for his particular compoistion is biocompatible[12], ferromagnetic and optical active.

A common, fast and cost-effective route to produce porous met-als is represented by the dealloying method. This process is based on the selective removal of the less noble atoms from the alloy, which eventually led to an interconnected network of pores and ligaments[13]. Most of the work on dealloying has been done on a bi-component, single phase, solid solution alloys, among which the most common are the Cu-Au[14], Au-Ag[15,16], Cu-Mn[17], and more, in general, the Al_xM_{100-x} alloys, where M=(Au, Pd, Pt, Ag and Cu)[18]. For what it concern the production of porous Pd or porous alloys of palladium, different system have been con-sidered, such as AlPd[18], PdCu[19,20], NiPd[21], PdCo[22,23], as well ternary systems have been studied for the synthesis of FePd NPs, like the FeAlPd[24] and AlPdNi[25].

In this work, single-phase polycrystalline $Fe_{75}Pd_{25}$ (at.%) alloy has been considered as starting material to produce nanoporous thin films via chemical dealloying. The initial stoichiometry, abundant in iron, guarantee to be far away from the parting lim-iting, hence, making it possible the dealloying process.

Results and discussion

Morphology and crystal structure

The evolution of the morphology of samples dealloyed for different times can be observed from scanning electron microscope (SEM) and atomic force microscope (AFM) images (Fig. 1 to Fig. 6). On the surface of as-prepared sample (Fig. 1 , t=0) small cracks can be recognised, most probably generated by the residual stresses determined during the deposition of the film[26]. However, the surface is smooth, with a roughness of (1.4 ± 0.2) nm (calculated according to[27,28]). From SEM image of the as prepared sample (see Fig. 1), it is evident the presence, besides cracks, of bumps on the surface that can be related to the presence of columnar crystalline grains, usually formed during sputtering deposition[26]. This interpretation can be confirmed from AFM image (see Fig. 1 (b)) where individual grains can be associated to the bumps on the surface of the sample. From GIXRD of the as-prepared sample (Fig. 7) it can be seen that the (110) reflection of the α-(Fe,Pd) has an anomalous shape due to the presence of a non homogeneous Pd content in the α-(Fe,Pd) supersaturated solid solution that enable the formation of a convolution of diffraction peaks at slightly different angles, each one related to a solid solution with a slightly different composition, i.e. slightly different lattice parameters. Therefore, an asymmetric reflection characterised by high full width at half maximum (FWHM) and a broad and rounded tip is obtained. From this evidence, areas characterised by different reduction voltages can be inferred due to the not uniform distribution of Fe and Pd in the crystalline grains of the α-(Fe,Pd) supersaturated solid solution. Areas with higher Pd content can be expected to be more noble with respect to regions with a reduced amount of Pd. Therefore, electrolyte is expected to act preferably on the less noble areas, starting the dealloying process where Fe content is higher. Moreover, at the beginning of the process, the electrolyte can penetrate into cracks present on the surface, therefore, Fe atoms will be firstly removed from the side of the cracks. From Fig. 2, t=15 minutes, cracks appears slightly enlarged and bumps, previously related to columnar crystalline grains, have voids surrounding them, hence, it can be observed that at the beginning, the dealloying process, is acting in cracks and at the grain boundaries. The (110) reflection of the α-(Fe,Pd) for 15 minutes sample has a different profile with respect to the as-prepared sample, that is, the peak becomes symmetric, the tip is sharp and the FWHM is reduced (see Fig. 7). This can be related to the dealloying of the less noble areas in the sample, with the dissolution of Fe and the consequent surface diffusion of Pd adatoms. As voids are created where grains boundaries are present, it can be inferred that grain boundaries are less noble then the core of the grains, i.e. they have an higher Fe content. Therefore, it can be inferred that, during sputtering, an increase in Fe content is produced from the core of the columnar crystals to the grain boundaries with a composition gradient. Therefore, when dealloying starts, Fe is removed preferentially from the side of the grains and the core, characterised by an uniform more noble composition, remains unaltered due to its higher electrochemical stability. This hypothesis is validated by the large decrease in Fe content after 15 minutes of dealloying down to

62% at.% as shown in Fig. 9. Furthermore, the roughness of the surface of the sample increases, reaching a value of (1.6 ± 0.2) nm, due to the dealloying acting preferentially on the grain boundaries. After 30 minutes of dealloying (see Fig. 3), the process is proceeding by increasing the deepness of the voids around the grains as it can be observed from the AFM image in which the grain morphology is similar to the 15 minutes sample, while the roughness is increased up (3.0 ± 0.3) nm as reported in Fig. 8. After 60 minutes, the iron content decreases further, reaching an atomic content of 60 % and the grain boundaries of the crystalline grains are well evident. At this stage, the dealloying is not only proceeding between cracks and in the grain boundaries, but starts to act also on the surface of the grains and ligaments start to be formed. This can be evidenced both from SEM and AFM images, and from a further increase in roughness up to (3.4 ± 0.3) nm. According to the model proposed by Erlebacher et al.[29], at this stage, palladium adatoms are diffusing on the surface, forming clusters that start to coalesce, giving rise to hill-shaped features on the surface. Simultaneously, the dissolution of the iron is proceeding, removing more atoms from the surface of the film.
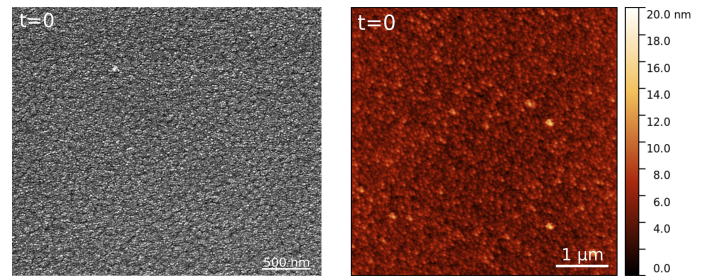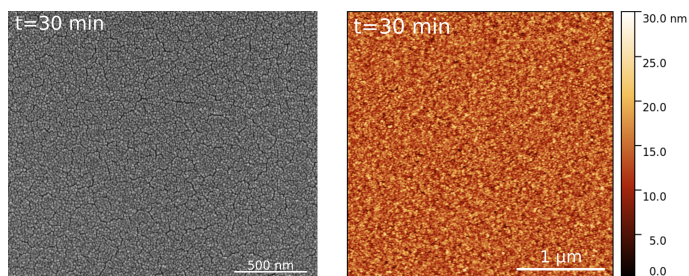

Fig. 1 SEM images (on the left) and AFM images (on the right) of the surface of the as prepared film.
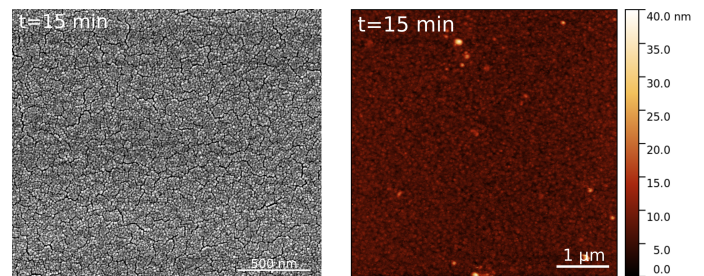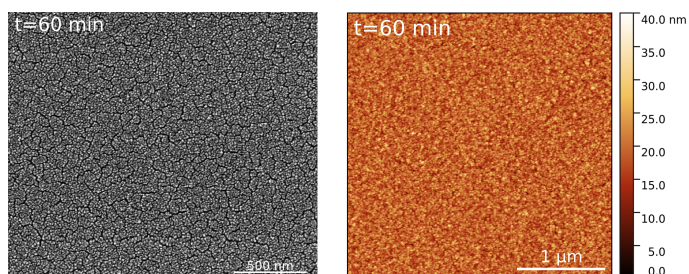

Fig. 2 SEM images (on the left) and AFM images (on the right) of the surface of the film dealloyed for 15 minutes.

Increasing the dealloying time up to 90 (see Fig. 5) and 120 minutes (see Fig. 6), a strong evolution of the surface morphology can be observed. This is due to the evolution of the dealloying process with the formation of an array of pores and ligaments which dimensions, well evident from SEM images (Fig 5), are increasing with the dealloying time (from 90 up to 120 minutes). At this stage (film dealloyed for 120 min), the surface roughness reaches its maximum, with a value of (6.6 ± 0.4) nm. However, in this phase, there is only a slight decrease in the average composition, with a decrease in Fe content that reaches a value of about 52%. As can be seen from the diffraction patterns of Fig.
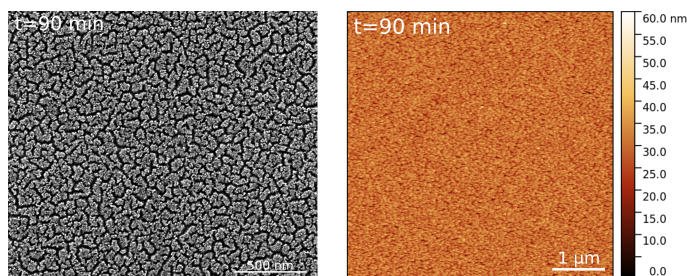
Fig. 3 SEM images (on the left) and AFM images (on the right) of the surface of the film dealloyed for 30 minutes.
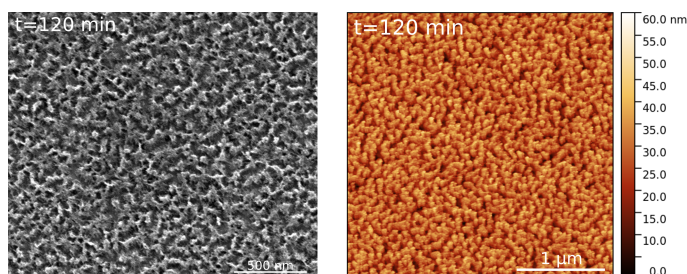

Fig. 4 SEM images (on the left) and AFM images (on the right) of the surface of the film dealloyed for 60 minutes.


Fig. 5 SEM images (on the left) and AFM images (on the right) of the surface of the film dealloyed for 90 minutes.

Fig. 6 SEM images (on the left) and AFM images (on the right) of the surface of the film dealloyed for 120 minutes.

7, for the film dealloyed for 120 minutes, besides the α-(Fe,Pd) solid solution, an additional face-centred cubic (FCC) phase is recognisable, belonging to a palladium rich phase. Comparing the angular position of the (200) reflection of a pure palladium phase (2θ=46.956) with the angular position of (200) reflection measured for the dealloyed film (2θ=47.204), it can be seen that it has a smaller lattice parameter, accounting for the presence of some Fe dissolved bi the Pd phase, which form a solid solution γ-(Fe,Pd). Moreover, the peak belonging to the γ-(Fe,Pd) phase presents a high FWHM which indicates for the formation of nanocrystalline grains. According to the observed trend of the alloy stoichiometry (Fig. 9), it can be seen that after 90 minutes of dealloying the composition remains almost unaltered. Therefore, the formation of a Pd rich passivation layer on the surface of the material can be inferred, that preserve the FePd solid solution still presents underneath from a further dealloying. The formation of the passivating layer could be related to the coalescence of the Pd clusters formed on the surface during the dealloying process. The formation of a passivation layer on the surface of a nanoporous sample was previously observed in literature for a Cu-Rh system in which an oxide passive layer was detected[30]. Liu *et al.* observed that the oxide passive layer was mainly constituted by the noble Rh element and stated that similar behaviour can be detected in alloys containing passive noble metals (such as Pt and Pd). On this basis, the formation of a Pd rich passivation layer is confirmed in Fe-Pd system. In the Fe-Pd system, a change in structure is observed from BCC α-(Fe,Pd) solid solution to FCC Pd rich phase. That is related to a process of nucleation and growth of a new phase[31] that is not observed when the starting alloy and the resulting nanoporous metal have the same crystal structure and similar lattice constants (i.e for example in well-known Au-Ag or Au-Cu systems[15]). In the latter case, ligament formation

can be explained by the surface diffusion of the more noble element on a rigid lattice that is followed by the adatoms in their diffusion, so that the original crystalline orientation of the grains is retained in the final ligament network. Still, the dealloying mechanism is much less understood for systems where a change of both crystalline structure and lattice constant is observed during dealloying. When a change in structure is acting, the more noble adatoms (Pd in this case) can nucleate clusters randomly oriented on the surface that can grow up to the impingement forming very fine nanocrystals. For Pd the surface mass transfer diffusion coefficient in vacuum is $1.1 \cdot 10^{-20}$ cm$^2 \cdot$ s^{-1} and much higher is expected at the alloy/electrolyte interfaces with an increase of four orders of magnitude[18]. Therefore, a high rate of diffusion is acting during dealloying, which enables the formation of a Pd passivation layer on the ligaments surface. According to the observed trend of the alloy stoichiometry (Fig. 9), it can be seen that the composition remains almost unaltered after 90 minutes of dealloying. Therefore, it can be expected that the passivation layer is already formed at that stage and it was growing in time. However, in the GIXRD patterns of Fig. 7, the presence of the palladium layer is recognisable only in the film dealloyed for 120 minutes. Most probably the thickness of the Pd passivation layer in the film dealloyed for 90 minutes was too thin to be detected by GIXRD.

After the film is dealloyed for 120 minutes (see Fig. 6), on the surface is recognizable a network of thin ligaments which dimension are in the range (20 ± 5) nm. Accordingly, the surface roughness increases reaching a value of (6.6 ± 0.4) nm, however, this value represents an underestimation because the radius of the AFM tip (which nominal value provided by the manufacturer is of 35 nm[32]) exceeds the dimension of the ligaments, hence the images are dominated by the convolution of ligaments and
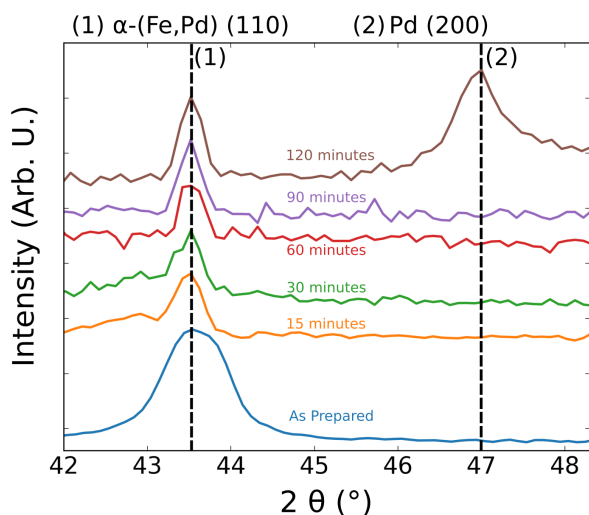
Fig. 7 GIXRD pattern for the dealloyed films at selected times for the angular range between 40 and 47 degree.

tip. The content of iron in the alloy reaches its minimum, with the final stoichiometry being of $Fe_{52}Pd_{48}$ (at. %). Nevertheless, this value represents an average between the Pd-rich passivation layer and the underlying part of the film, which will contain a lower amount of iron as compared to the one reported.
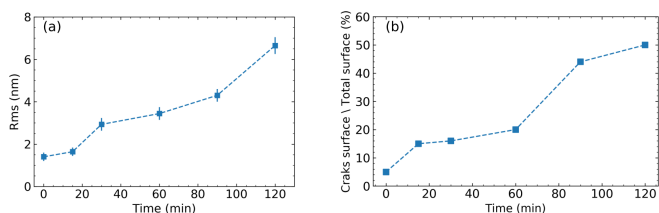

Fig. 8 Evolution (a) of the surface roughness as a function of the dealloying time and (b) of the ratio between cracks and materials surfaces as a function of the dealloying time.
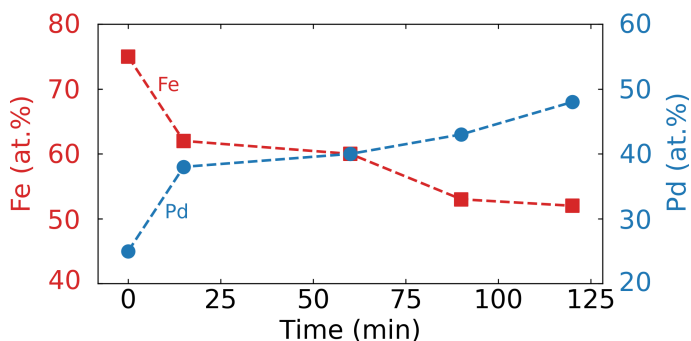
Fig. 9 Evolution of the stoichiometry of the alloy as a function of the dealloying time

Magnetic characterisation

The evolution of the magnetic properties of the dealloyed films has been investigated via vibrating sample magnetometer (VSM), recording hysteresis loop at room temperature both for the in-plane and for the out-of-plane direction, as shown in Fig. 10 panels (a)-(d). The hysteresis loop for the as-prepared sample, for the in-plane direction, shows a typical soft magnetic behaviour, with a single irreversible jump of the magnetisation, low coercive field ($H_c \simeq 65$ Oe) and a high susceptibility at coercive field ($\chi_c^{in} = 3.08 \cdot 10^{-5}$ emu·Oe^{-1}, where the apex *in* indicates the in-plane direction). Conversely, along the out-of-plane direction, the reversal of the magnetisation occurs mainly through reversible mechanism, requiring a field as high as 12 kOe to reach saturation, as well the susceptibility at coercive field is almost two orders of magnitude lower of the one for the in-plane direction ($\chi_C^{out} = 2.15 \cdot 10^{-7}$ emu·Oe^{-1}, where the apex *out* indicates for the out of plane direction). Hence, for the as-prepared films, the easy axis of magnetisation lies on the film plane, whereas the direction perpendicular to the film plane represents a hard axis for the magnetisation. The dealloying process causes an evolution of magnetic properties, such as magnetic moment, anisotropy and coercive field, as can be seen in Fig. 11 (a) and (b). From the data reported in the graph of Fig. 11 (a), it can be seen that the value of the magnetic moment of the films decreases as the dealloying time increases; after 60 minutes of dealloying, the magnetic moment of the films drops to almost 80 % of its initial value.
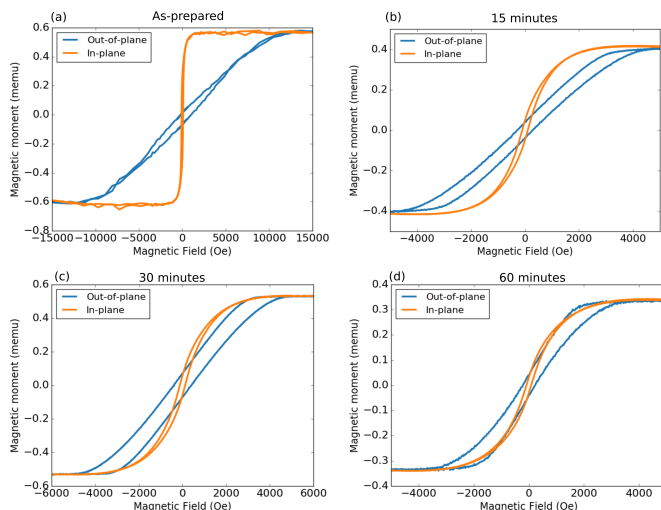
Fig. 10 Comparison between the in-plane and out-of-plane hysteresis loops for the (a) as-prepares film, (b) film dealloyed for 15 minutes, (c) film dealloyed for 30 minutes, (d) film dealloyed for 60 minutes.

The main mechanism that determines such loss is intrinsic in the dealloying process, which selectively removes the less noble atoms from the alloys, that in this particular case are the iron atoms, which give the ferromagnetic behaviours to the alloy. However, only the depletion of the iron atoms (see Fig. 9) does not justify for the 60 % loss of magnetic moment after only 15 minutes of dealloying. Indeed, it has to be taken into account that part of the film gets lost during the process. Considering the ratio between the area of the trenches and the area of the film, it

is possible to estimate the percentage of material loss during the process, as shown in Fig. 8 (b). With this approach, the material losses are underestimated, since it takes into account only the surface and not the volume of the films. Looking at Fig. 11 (a) it can be noticed that the decrease of magnetic moment at shorter times is more pronounced as compared to the one at longer times. This behaviour can be described considering that the onset of the dealloying process are the grains boundaries, which, as discussed before, are rich in Fe. Hence, a great part of the Fe gets lost in the first moment of the process. Another fact that is evident from the GIXRD pattern of Fig. 7, is the formation of a palladium-rich phase, which eventually passivates the film surface preventing further dealloying. The formation of this γ-(Fe,Pd) phase determines a decrease of the magnetic moment carried by the Fe atoms[33]. The combination of the depletion of the iron atoms, the loss of material and the formation of the γ-(Fe,Pd) phase, causes the reduction of the magnetic moment of the film during the dealloying process. As well the value of the coercive field is influenced by the dealloying process. From the graph reported in Fig. 11 (a), it can be seen that it reaches a maximum value of $H_c \approx 120$ Oe for the film dealloyed for 30 minutes, afterwards, its value decreases by increasing the dealloying time. This trend is determined by the process of grain refinement that took place as a consequence of the dealloying process[34]. Indeed, as pointed out in the previous discussion, the preferential sites for the dealloying process are the grain boundaries. Therefore, the grain dimension decreases during the dealloying, determining, from the magnetic point of view, an hardening of the material. However, this effect of magnetic hardening does not have a monotonic trend, indeed, the coercive field drops when dealloying the films for more than 30 minutes. The transition from a continuous to a nanoporous system, strongly influence the magnetic anisotropy of the system. Indeed, looking the loops along the out-of-plane direction reported in Fig. 10 (a) - (d), it can be seen how the sample, which in its as-prepared state is strongly anisotropic, acquire a more isotropic behaviour after dealloying. In Fig. 10, a more detailed com-
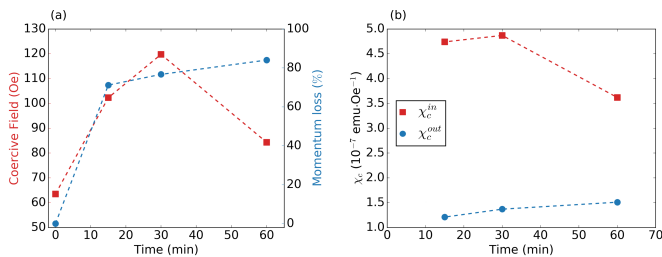

Fig. 11 Evolution of: (a) the coercive field (in red) and percent loss of magnetic moment (in red) for the in-plane direction for dealloyed films, (b) the value of the susceptibility at coercive field for the in-plane (in red) and out-of-plane (in blue) for dealloyed films.

parison between the in-plane and out-of-plane hysteresis loop of the films dealloyed at different times is reported. In this regard, another parameter that has been investigated is the evolution of the susceptibility at coercive field which is shown both for the in-plane (χ_c^{in}) and for the out-of-plane (χ_c^{out}) direction, which is reported in Fig.11 (b). As can be seen, by the trend of the χ_c^{out}, its

value increases as increasing the dealloying time, meaning that the system is becoming more and more isotropic. Conversely, the value for the susceptibility at coercive field for the in-plane direction decreases with time. Nevertheless, the two values get closer to each other, underlying once more that the system is acquiring a more isotropic behaviour, since the two values, for a fully isotropic system coincide. The films dealloyed at 90 and 120 minutes were not taken into account because of the reduced intensity of the magnetic moment, which makes the signal of the probe and of the substrate prevail on the ferromagnetic signal of the films.

Surface enhanced Raman scattering

Meso- and nanoporous meta-materials have shown the potentiality to be used as SERS-active substrates[10]. In particular, to the best of our knowledge, there are no studies analysing Pd-rich nanoporous materials as SERS-active substrates, even if the palladium should present harmonic oscillation of conduction electron on the surface, which will locally enhance the magnitude of the electric field, with the consequence to enhance the Raman scattering of several orders of magnitude. Here, we analysed the
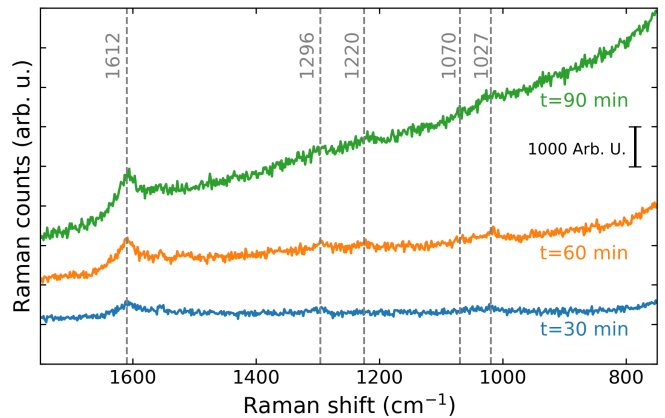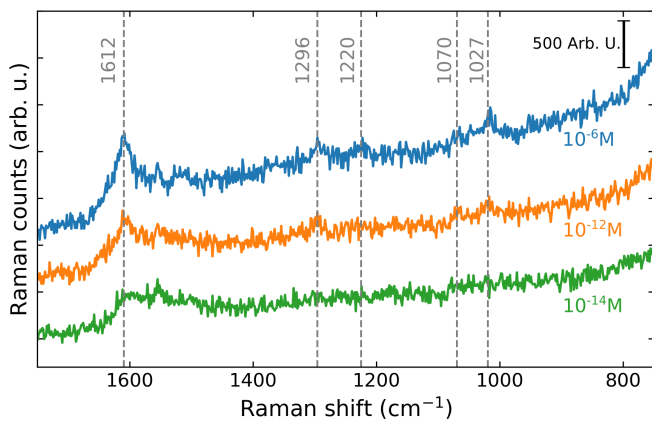

Fig. 12 Comparison of the SERS response for sample dealloyed in 2M HCl for (a) 30 minutes, (b) 60 minutes and (c) 90 minutes, incubated for 1 hour in a 10^{-6}M ethanol solution of bipyridine.

presence of SERS enhancement for the different samples. Indeed, as seen so far, the superficial structure of the sample evolves as a function of the dealloying time, going from a smooth surface to a rough surface with the presence of ligaments and pores. As probe molecule, we use a standard bipyridine in ethanol solution with different concentration. Firstly, the effect of different dealloying time on the SERS effect has been investigated for the detection of a fixed concentration of bipyridine of 10^{-6} M and the acquired spectra are reported in Figure 12. The only visible peak, that may be ascribed to the bipyridine is the one at 1613 cm^{-1}. Looking at the spectrum of Fig.12 (b), for the sample dealloyed for 60 minutes, the intensity of the peak at 1613 cm^{-1} increases. Moreover, other peaks (as indicated in the graph) are appearing in the spectrum. The same consideration can be done on the spectrum (c) of Fig. 12, relative to the sample dealloyed for 90 minutes. Increasing the dealloying time, a broad, monotonic feature appears as a baseline at lower energies. Interestingly, the morphology of

the samples surface becomes coarser and coarser when dealloying proceeds (Figs. 2-6). At the beginning, pores diameter is still below the wavelength of visibile light, meaning that the last *sees* the sample as an effective homogeneous medium, whereas scattering can occur for heavy dealloyed samples, being the pores several tens nanometer wide. The increased Raleigh scattering from the excitation laser is then the origin for baseline here observed. The situation recalls that of nano- and meso-porous Si[35] as opposed to macro-porous Si[36].

Being the spectrum of the sample dealloyed for 60 minutes the most resolved, and the one which presents the higher intensity of the peak at 1613 cm^{-1}, we proceed to analyse the effect of different concentration of the bipyridine molecule on the sample dealloyed for 60 minutes. The acquired spectra are shown in Fig. 13. Decreasing the bipyridine concentration of 6 order of magnitude, a noticeable SERS enhancement is still visible. However, the spectrum becomes almost flat for a concentration of 10^{-14} M. Hence, these kind of substrates are suitable to detect bipyridine in concentrations as low as 10^{-12} M.

Fig. 13 Comparison of the SERS response for sample dealloyed for 1 hour, incubated in different concentration of bipyridine.

Conclusions

Pd-rich nanoporous thin films were fabricated via chemical dealloying from single phase polycrystalline Fe$_{75}$Pd$_{25}$ (at. %) continuous thin films produced via confocal sputtering. The master alloy in its as-prepared state is a polycrystalline supersaturated solid solution of α-(Fe,Pd) with a body-centered cubic structure. The dealloying was carried out immersing the films in a 2 molar aqueous solution of HCl at room temperature for different times. The stoichiometry of the alloy's decays exponentially in time, showing an asymptotic behavior for times longer than 90 minutes, where a stoichiometry of Fe$_{52}$Pd$_{48}$ is reached. The removal of the less noble element generates adatoms of palladium on the film surface, which diffuses towards each-others to form clusters which eventually coalesce forming a passivation layer which hinders the dealloying process. The morphology of the films evolves as a function of the dealloying time. In its as-prepared state, the films show the presence of fractures on the surface, ascribable to the presence of

residual stresses. Those trenches, which represent as well grain boundaries, represent a preferential on-set for the dealloying process. The evolution in time of the magnetic properties of the film has been investigated at room temperature for the in-plane and out-of-plane direction of the magnetic field. The sample, in its as-prepared state is characterized by a soft magnetic behavior and a strong anisotropy, with the easy axes of magnetization lying on the film plane. During dealloying, iron atoms are removed from the alloy, hence the magnetic moment of the film decreases during the dealloying. Contemporary, the crystalline grains, undergo a refinement process that influences the coercive field which increases at short dealloying times and then decreases again for longer dealloying times. Evolving from a continuous towards a nanostructured system, as well the magnetic anisotropy gets influenced by the dealloying process, which confers to the film a more isotropic behavior. Finally, thin films dealloyed at different times were investigated as surface-enhanced Raman spectroscopy substrates, using bipyridine as a probe molecule. The as-prepared film does not show any SERS effect, while dealloyed films show an enhancement in the Raman signal related to the bipyridine. The higher enhancement has been found for the sample dealloyed for 60 minutes. Most probably, in this case, the dimension of the palladium clusters formed on the surface determines the proper spatial confinement which generates surface plasmons which in turn determine the enhancement of the Raman signal.

Experimental

The deposition of thin film of Fe$_{75}$Pd$_{25}$ (at.%) was performed via dual source sputtering (P$_{base}$ = 1.0 · 10^{-7} mbar) in an argon atmosphere (P$_{dep}$ = 1.0 · 10^{-2} mbar) . Two different targets of elemental iron (purity 99.99%) and elemental palladium (purity 99.98%) were used in a confocal configuration, with the iron target driven at radio frequency and the palladium target driven with a continuous current. The thickness of the as prepared films, measured via atomic force microscopy (AFM), is of (100 ± 2) nm. The FePd films were deposited on a gold-coated silicon oxide substrate and subsequently chemically dealloyed in a 2 molar aqueous solution of hydrochloric acid, without applying any external potential. In this regime, since the pH of the electrolyte is almost zero, according to the Pourbaix diagrams at room temperature[37], the iron gets corroded, while being in the immunity region for the palladium, avoiding the formation of palladium hydrides. All the dealloying experiments were carried out at room temperature and without stirring the solution. Samples were dealloyed for selected times, ranging from 15 minutes up to 120 minutes. To interrupt the action of the etching solution, the samples where rinsed repeatedly with de-ionised water. The evolution of the morphology and of the stoichiometry was studied via scanning electron microscopy (SEM) equipped with a energy dispersive x-ray spectrometer (EDS) and with atomic force microscopy (AFM). Analysis of the SEM images was performed using the ImageJ software[38]. The crystal structure of the films, for selected dealloying times, has been investigated via grazing incidence x-ray diffraction (GIXRD) using the Cu-K$_\alpha$ radiation. The magnetic properties were investigated at room temperature using a vibrating sample magnetometer (VSM) capable to provide

a maximum field of 20 kOe and equipped with a rotating head, used to investigate the magnetic anisotropy of the samples. The dealloyed samples were studied as well as a substrate for Surface Enhanced Raman Scattering (SERS). SERS measurements were performed with a Renishaw inVia Raman Microscope, equipped with a 514 nm wavelength laser line. The optimised experimental conditions were defined as an acquisition time of 40 s, 100% power at the surface and a 20x magnification objective. Before experiment, samples were deeply cleaned in de-ionised water to remove traces of acids from pores and then dried at air. As a probe molecule, 4-4 bipyridine (bipy) in ethanol solution with concentrations ranging from 10^{-6} to 10^{-14} M. The samples were incubated for one hour into the solution with the desired concentration of bipy, then dried at air, and subsequently measured. All the solutions were prepared from reagents grade chemicals and de-ionised water.

Conflicts of interest

There are no conflicts to declare.

Acknowledgements

Notes and references

1 L. H. Qian, A. Inoue and M. W. Chen, *Applied Physics Letters*, 2008, **92**, 1–4.

2 M. W. Verbrugge and P. Liu, *Journal of The Electrochemical Society*, 2005, **152**, D79.

3 J. Liu and X. W. Liu, *Advanced Materials*, 2012, **24**, 4097–4111.

4 F. Scaglione, Y. Xue, F. Celegato, P. Rizzi and L. Battezzati, *Journal of Materials Science*, 2018, **53**, 12388–12398.

5 E. M. Paschalidou, F. Scaglione, A. Gebert, S. Oswald, P. Rizzi and L. Battezzati, *Journal of Alloys and Compounds*, 2016, **667**, 302–309.

6 F. Scaglione, E. Alladio, A. Damin, F. Turci, C. Baggiani, C. Giovannoli, S. Bordiga, L. Battezzati and P. Rizzi, *Sensors and Actuators B: Chemical*, 2019, **288**, 460–468.

7 Y. Xue, S. Wang, P. Shi, Y. Huang, F. Scaglione, P. Rizzi, L. Battezzati, P. Denis and H.-J. Fecht, *Chemical Physics Letters*, 2019, **723**, 22–27.

8 A. Quintana, J. Zhang, E. Isarain-Chávez, E. Menéndez, R. Cuadrado, R. Robles, M. D. Baró, M. Guerrero, S. Pané, B. J. Nelson, C. M. Müller, P. Ordejón, J. Nogués, E. Pellicer and J. Sort, *Advanced Functional Materials*, 2017, **27**, 1701904.

9 Y. Xue, F. Scaglione, E. M. Paschalidou, P. Rizzi and L. Battezzati, *Chemical Physics Letters*, 2016, **665**, 6 – 9.

10 X. Zhang, Y. Zheng, X. Liu, L. Wei, J. Dai, D. Lei and D. MacFarlane, *Advanced Materials*, 2015, **27**, 1090–1096.

11 Y. Xue, F. Scaglione, P. Rizzi and L. Battezzati, *Applied Surface Science*, 2017, **426**, 1113–1120.

12 Y. Ma, M. Zink and S. G. Mayr, *Applied Physics Letters*, 2010, **96**, 213703.

13 J. Erlebacher and R. Seshadri, *MRS Bulletin*, 2009, **34**, 561–568.

14 R. Morrish, K. Dorame and A. Muscat, *Scripta Materialia*, 2011, **64**, 856–859.

15 J. Erlebacher, M. J. Aziz, A. Karma, N. Dimitrov and K. Sieradzki, *Nature*, 2001, **410**, 450–453.

16 X. Lu, E. Bischoff, R. Spolenak and T. Balk, *Scripta Materialia*, 2007, **56**, 557–560.

17 J. Hayes, A. Hodge, J. Biener, A. Hamza and K. Sieradzki, *Journal of Materials Research*, 2006, **21**, 2611–2616.

18 Z. Zhang, Y. Wang, Z. Qi, W. Zhang, J. Qin and J. Frenzel, *Journal of Physical Chemistry C*, 2009, **113**, 12629–12636.

19 S. Shan, J. Markmann and J. Weissmüller, *Philosophical Magazine*, 2017, **97**, 1571–1587.

20 S. Shan, J. Markmann and J. Weissmüller, *Electrochimica Acta*, 2018, **285**, 60 – 69.

21 L. Chen, H. Guo, T. Fujita, A. Hirata, W. Zhang, A. Inoue and M. Chen, *Advanced Functional Materials*, 2011, **21**, 4364–4370.

22 M. Hakamada and M. Mabuchi, *Journal of Alloys and Compounds*, 2009, **479**, 326 – 329.

23 M. Goessler, M. Albu, G. Klinser, E.-M. Steyskal, H. Krenn and R. Würschum, *Small*, 2019, **15**, 1904523.

24 J. Wang, Z. Wang, D. Zhao and C. Xu, *Analytica Chimica Acta*, 2014, **832**, 34 – 43.

25 Z. Qi, H. Geng, X. Wang, C. Zhao, H. Ji, C. Zhang, J. Xu and Z. Zhang, *Journal of Power Sources*, 2011, **196**, 5823 – 5828.

26 J. A. Thornton, *Journal of Vacuum Science and Technology*, 1975, **12**, 830–835.

27 P. K. D. Necas, *Central European Journal of Physics*, 2012, **10**, 118–188.

28 P. Klapetek, *Quantitative Data Processing in Scanning Probe Microscopy*, William Andrew, 2012.

29 J. Erlebacher, M. J. Aziz, A. Karma, N. Dimitrov and K. Sieradzki, *Nature*, 2001, **410**, 450–453.

30 F. Liu and H.-J. Jin, *Journal of The Electrochemical Society*, 2018, **165**, C999–C1006.

31 E. Paschalidou, F. Celegato, F. Scaglione, P. Rizzi, L. Battezzati, A. Gebert, S. Oswald, U. Wolff, L. Mihaylov and T. Spassov, *Acta Materialia*, 2016, **119**, 177–183.

32 Bruker, *AFM probes Mesp-HR10*, 2019, `https://www.brukerafmprobes.com/p-3413-mesp-hr10.aspx`.

33 K. Adachi, D. Bonnenberg, J. J. M. Franse, R. Gersdorf, K. A. Hempel, K. Kanematsu, S. Misawa, M. Shiga, M. B. Stearns and H. P. J. Wijn, *Numerical Data and Functional Relationships in Science and Technology*, Springer, 1986.

34 E. Arzt, *Acta Materialia*, 1998, **46**, 5611–5626.

35 G. G.Amato, G. Benedetto, L. Boarino, G. Lérondel, M. Rossi and R. Spagnolo, in *Semiconductors and Electronic Materials*, ed. P. H. A. Mandelis, SPIE, Bellingham, 2000, ch. Photothermal and photoacoustic characterization of porous silicon structures.

36 G. Amato, *Japanese Journal of Applied Physics*, 1995, **34**, 1716–1722.

37 M. Pourbaix, *Atlas d'Equilibres Electrochimiques*, Gauthier-Villars, 1963.

38 C. A. Schneider, W. S. Rasband and K. W. Eliceiri, *Nature methods*, 2012, **9**, 671–675.